ANALYSIS OF JET SHEAR LAYER SELF-SUSTAINED INSTABILITY EFFECTS ON THE INFLOW CONDITIONS

Carlos A.S. Moser
Pontícia Universidade Católica do Rio Grande do Sul, Porto Alegre-RS, 90619-900, Brazil
carlos.moser@yahoo.com.br

Marcello A.F. Medeiros
Universidade de São Paulo, São Carlos-SP, 13560-970, Brazil
marcello@sc-usp.br

Abstract. *The noise radiated by a Mach 0.9 isothermal jet at Reynolds number 65,000 (based on the jet diameter) was investigated by an implicit large-eddy simulation method. By this approach, flow and sound propagation were directly computed without any modeling assumption. Flow variables were solved by the compressible Navier-Stokes equations written in a non-conservative form. As main advantages, this formulation reduces the sensitivity to aliasing errors and avoids Favre averaging of flow variables, providing strong nonlinear stability for high-order compact schemes. Sixth-order compact finite difference schemes were used for spatial discretization and filtering. Implicit filters were applied to the flow variables to suppress high-frequency oscillations provided by unresolved scales, mesh non-uniformities and boundary conditions. Boundary conditions and buffer zone treatments were prescribed by a characteristic-based formulation and a conceptual model based on the characteristic analysis. In this study, the jet basic flow was kept unforced close to the inlet in order to investigate the influence on the aerodynamic noise radiation of exponentially growing self-sustained instabilities developed in the jet shear-layer. A feed-back mechanism induced by close interactions of vortices formed in the shear layer was identified.*

Keywords: *Computational aeroacoustics; Implicit Large-eddy simulation; Subsonic jet; Shear layer instability.*

1. INTRODUCTION

Nowadays, the world-wide aircraft and jet engine industries are facing increasingly stringent noise regulations requirements to reduce noise annoyance due to the near-airport aircraft flight operations. Regardless of significant advances in the noise predictive capabilities, the complete understanding of the unsteady flow-noise generation phenomena remains one of the most important challenges in the design of more silent aircrafts. Further improvements on the fidelity of noise prediction tools used to aid in the airframe/engine design process require a deeper physical-based insight into the multi-scale dynamics of the unsteady flow-noise generation phenomena. Noise prediction tools must be conceived to capture a wide range of scales of turbulence for accurately predict the broad-banded energy spectrum of the audible sound.

Among the classical approaches commonly used for unsteady flow-noise predictions, the Direct Numerical Simulation (DNS) is the only one that can provide the complete description of flow-noise source and sound propagation by solving directly and simultaneously all scales of the flow. The DNS also provides highly-accurate data for the development and validation of turbulence models for noise prediction methods, such as Large-Eddy Simulation (LES) and Reynolds Averaged Naviers-Stokes (RANS). However, its application has been restricted to low Reynolds number flows and relatively simple geometries, due to its prohibitively high computational cost. Unlike the DNS, the LES and RANS methods can be employed for noise predictions of high-Reynolds-number flows at lower computational cost. By RANS-based models, unsteady fluctuations are time-averaged in the attempt to obtain an equivalent noise source distribution based on mean flow properties. Nevertheless, the empiricism of the simplified noise source terms significantly reduces the effectiveness of this approach in accurately capture noise levels and sound directivity (Bodony, D. J. and Lele, S. K., 2002). By large-eddy simulation, the large-scale energy containing eddies are filtered, while the small unresolved subfilter scales are modeled or reconstructed in some appropriate fashion.

In the present study, alternatively to the traditional LES methods based on eddy-viscosity type models (Germano, M. and Piomelli, U. and Moin, P., 1991), was developed and validated an implicit LES method based on the Approximate Deconvolution Model (ADM) (Stolz, S. and Adams, N. A., 1999) and a non-conservative form of flow equations. The basis of the LES/ADM approach is that truncation errors associated to the numerical discretization have similar form or action to the subgrid scales. Such approach lies in the class of structural models, since the subgrid scales are completely determined by the structure of the resolved scales of the flow (Sagaut, P., 2001). As this approach does not require additional subgrid-scale stress or heat flux terms in the flow equations, flow-noise source and sound propagation may be directly computed without the need of any subgrid-scale modeling assumption. The non-conservative form of the fully compressible Navier-Stokes equations was used to solve the flow variables (pressure, velocity and entropy) for modeling in an appropriated fashion unsteady flows with rapid property variations, such as compressible free-shear layers. As

main advantages, the non-conservative form avoids the density weighting (Favre averaging) of flow variables and also reduces the sensitivity to aliasing errors, providing strong nonlinear stability for high-order non-dissipative compact finite difference schemes (Lele, S. K., 1992). As drawback, it is unsuitable for flows involving shocks, since the momentun and total energy are not conserved.

2. NUMERICAL METHOD

2.1 Flow governing equations

The compressible Navier-Stokes equations written in the non-conservative form was used to solve the flow variables in Cartesian coordinates as follows

$$\frac{\partial p}{\partial t} = -\left(u\frac{\partial p}{\partial x} + v\frac{\partial p}{\partial y} + w\frac{\partial p}{\partial z}\right) - \rho c^2\left(\frac{\partial u}{\partial x} + \frac{\partial v}{\partial y} + \frac{\partial w}{\partial z}\right) + (\gamma - 1)\left(-\frac{\partial q_i}{\partial x_i} + \Phi\right) \tag{1}$$

$$\frac{\partial u}{\partial t} = -\left(u\frac{\partial u}{\partial x} + v\frac{\partial u}{\partial y} + w\frac{\partial u}{\partial z} + \frac{1}{\rho}\frac{\partial p}{\partial x}\right) + \frac{1}{\rho}\frac{\partial \tau_{1j}}{\partial x_j} \tag{2}$$

$$\frac{\partial v}{\partial t} = -\left(u\frac{\partial v}{\partial x} + v\frac{\partial v}{\partial y} + w\frac{\partial v}{\partial z} + \frac{1}{\rho}\frac{\partial p}{\partial y}\right) + \frac{1}{\rho}\frac{\partial \tau_{2j}}{\partial x_j} \tag{3}$$

$$\frac{\partial w}{\partial t} = -\left(u\frac{\partial w}{\partial x} + v\frac{\partial w}{\partial y} + w\frac{\partial w}{\partial z} + \frac{1}{\rho}\frac{\partial p}{\partial z}\right) + \frac{1}{\rho}\frac{\partial \tau_{3j}}{\partial x_j} \tag{4}$$

$$\frac{\partial s}{\partial t} = -\left(u\frac{\partial s}{\partial x} + v\frac{\partial s}{\partial y} + w\frac{\partial s}{\partial z}\right) + \frac{R}{p}\left(-\frac{\partial q_i}{\partial x_i} + \Phi\right) \tag{5}$$

In the system of equations above, p denotes the pressure, u, v and w the velocity components and s the entropy. q_i represents the heat flux modeled by the Fourier's law of heat conduction, Φ the viscous dissipation and τ_{ij} the viscous stress tensor. For simplicity, the fluid was assumed to be a calorically perfect gas with constant molecular properties. Thus, the system of equations may be closed by the following thermodynamic relations for an ideal gas

$$\rho = p^{1/\gamma}e^{-s/C_p}, \quad T = \frac{p}{\rho R} \quad \text{and} \quad c^2 = \frac{\gamma p}{\rho} \tag{6}$$

where ρ, T and c represent, respectively, the density, temperature and sound speed. $R = C_p - C_v$ is the universal gas constant and $\gamma = C_p/C_v$ the ratio of specific heats at constant pressure and volume.

2.2 Implicit large-eddy simulation

In this work was developed an implicit Large-Eddy Simulation (LES) method which combines high-order implicit filtering of flow variables with an Approximate Deconvolution Model (ADM) (Stolz, S. and Adams, N. A., 1999). The implicit filtering of flow variables was applied to suppress high-frequency instabilities which arise from coarse grid resolution, mesh non-uniformities, unresolved scales and boundary conditions, providing dissipation only to the higher wavenumbers, where the spatial discretization already exhibits significant dissipation errors. The deconvolution model was employed to reconstruct the effect of subfilter scales in the unfiltered flow solution. Thus, dissipation errors produced by the numerical method may be restricted to a relatively narrow range of the highest wavenumbers. The filtering of the flow variables in the physical space was defined by Leonard, A. (1974) as follows

$$\bar{f}(x) = \int_\Omega f(x')G(x, x'; \delta)dx' \tag{7}$$

where Ω is the entire domain, G the filter kernel and δ the filter width associated to the smaller scales retained by the filtering operation. The filtering operation defines the size and structure of the smaller scales of the flow. At the boundary points $i = 1$ and N the flow variables were kept without filtering, while at the interior of domain, for points $i = 4, ..., N - 3$, the flow variables were filtered sequentially in each spatial direction at the final stage of each time step with sixth-order accurate implicit filters (Gaitonde, D. V. and Visbal, M. R., 1999) defined by

$$\alpha_f \bar{f}_{i-1} + \bar{f}_i + \alpha_f \bar{f}_{i+1} = \sum_{n=1}^{4} \frac{a_n}{2}(f_{i-n+1} + f_{i+n-1}) \tag{8}$$

where the coefficients a_n were derived by the analysis Taylor and Fourier series (Gaitonde, D. V. and Visbal, M. R., 1998, 1999) in terms of the filtering parameter α_f defined at the interval $[-0.5, 0.5]$. For $\alpha_f = 0.5$ there is no filtering effect. By contrast, for $\alpha_f = 0$ the explicit filtering presents significant degradation of the spectral frequency response. In this study the filtering parameter α_f was set to 0.4.

As the Eq. (8) has a stencil of seven points, it cannot by employed near to the boundaries of the domain. Thus, the following implicit filtering operation was used at points $i = 2$ and 3:

$$\alpha_f \bar{f}_{i-1} + \bar{f}_i + \alpha_f \bar{f}_{i+1} = \sum_{n=1}^{7} a_{n,i} f_n \tag{9}$$

and, analogously, at the points $i = N - 2$ and $N - 1$.

The Approximate Deconvolution Model (ADM) (Stolz, S. and Adams, N. A., 1999) was used to compute an approximation of the unfiltered solution f from the filtered solution $\bar{f}$ as follows:

$$\bar{f} = G * f = \int G(x - x') f(x') dx' \tag{10}$$

If the filter transfer function G has an inverse Q, then an approximation of the unfiltered variable, denoted by f^*, may be obtained by the deconvolution of the filtered variable.

$$f^* = Q * \bar{f} \tag{11}$$

where the inverse filter transfer function Q may be obtained by the truncated Taylor series expansion

$$Q_N = \sum_{\nu=0}^{N} (I - G)^\nu \tag{12}$$

where I is the identity matrix and $N = 1, 2, 3, ...$ the number of time steps. The family of the inverse filtering functions Q_N is based on an iterative method (Galdi, G. P., 2000). High-order approximations f^* of the variable f were derived by applying successive filtering operations to the filtered quantities

$$f^* = \bar{f} + (I - G) * \bar{f} + (I - G) * ((I - G) * \bar{f}) + ... \tag{13}$$

In smooth regions of the flow these filters present stabilizing properties and high-order consistency errors $O(\delta^{2N+2})$, where δ is the filter width. According to Stolz, S. and Adams, N. A. (1999), the order of truncation of Eq. (13) determine the level of deconvolution. Here we adopt a third level quadratic extrapolation

$$f^* \approx Q_2 \bar{f} := 3\bar{f} - 3\bar{\bar{f}} + \bar{\bar{\bar{f}}} \tag{14}$$

since it affords sixth-order consistency error, $O(\delta^6)$.

2.3 Message passing interface multi-block parallel solver

In this study, a Message Passing Interface (MPI) multi-block parallel strategy was deemed in the attempt to preserve the high-order of accuracy of the numerical schemes employed at the interfaces, since the accurate data transfer at the interfaces is of fundamental importance on noise predictions. In order to reduce memory allocation and communication time, each working process was initialized by the master process with your respective portion of the original single-block domain. Therefore, the multi-block parallel solver needs only to allocate memory to the block which is being currently initialized by the master process. As the memory allocated by each working process is inversely proportional to the total number of blocks decomposed, this procedure substantially reduces the need of memory allocation, especially for 3-D computations.

In order to illustrate the data transfer at the inter-block interface, a single block domain was decomposed in Fig. 1 into two adjacent blocks $L - 1$ and L with 9 points *overlap* interface. In the attempt to preserve at the interface the high-order of accuracy of the original numerical scheme applied to the single-block domain, the flow solution at points 1 to 4 of block L was transferred from points $N - 8$ to $N - 5$ of block $L - 1$. Similarly, the flow solution at points 6 to 9 of block L was transferred from points $N - 3$ to N of block $L - 1$. The arrows indicate the direction of data transfer in each point at the interface, except at middle points (5 and $N - 4$), which were computed independently in each block and, consequently, does not transfer data. The double solution at these points was used to detect possible deviations of the flow solution at the interface, since it was advanced independently in each adjacent block. The data transfer at the inter-block interface was performed at the final stage of the Runge-Kutta time advancement, as well as after applying the implicit filtering operation.

The effect of the *overlap* interface extent on accuracy of data transfer between blocks was evaluated by the analysis of the maximum root-mean-square (R.M.S) error of u-velocity, given by the difference of values computed by parallel MPI multi-block domain decomposition and single block domain (serial computation), taken as the reference solution. As shown in Fig. 2, the maximum R.M.S error of u-velocity at the interface was reduced in two orders of magnitude by increasing the *overlap* stencil from 9 to 13 points. Although, inter-block interfaces with larger *overlap* stencils have shown to be more accurate, they significantly increase the memory allocation, data processing and inter-block communication. Thus, in this study we chose to adopt inter-block interfaces with 13 points of *overlap*.
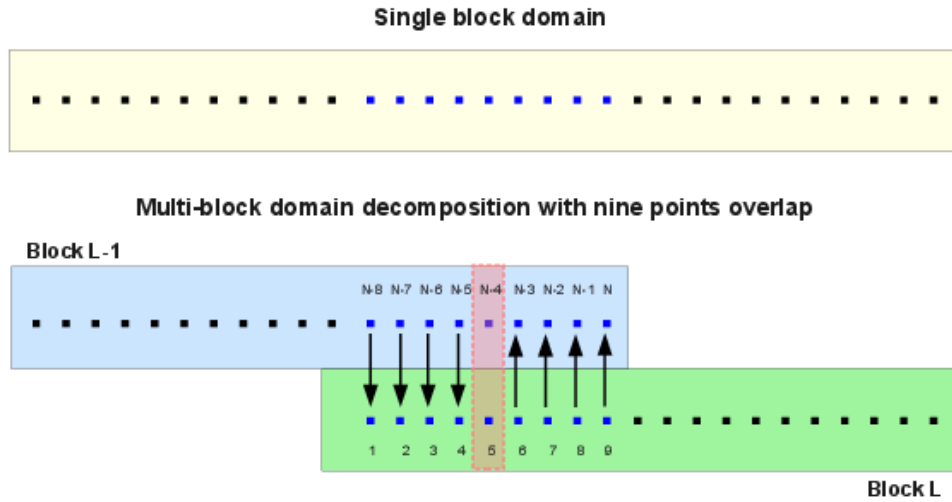
Single block domain

Multi-block domain decomposition with nine points overlap

Block L-1

N-8 N-7 N-6 N-5 N-4 N-3 N-2 N-1 N

1 2 3 4 5 6 7 8 9

Block L

Figure 1. **Single-block decomposed into two adjacent blocks** $L-1$ **and** L **with 9 points** *overlap* **interface. The arrows indicate the direction of data transfer between blocks, except at the middle points (5 and** $N-4$**), where the flow solution was advanced independently in each block.**
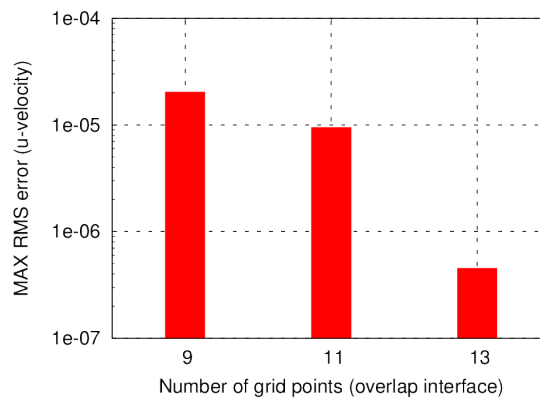
Figure 2.   **Maximum root-mean-square (R.M.S) error of u-velocity computed by multi-block decomposition relative to the single block solution. Inter-block interfaces with different overlap stencils: 9, 11 and 13 points.**

3. FLOW CONFIGURATION

In the present implicit LES, the jet nozzle exit was modeled by imposing at the inflow boundary of computational domain the following hyperbolic-tangent mean velocity profile

$$u(r) = \frac{U_j}{2}\left(1 + \tanh\left(\frac{r_o - r}{2\theta}\right)\right) \tag{15}$$

where U_j is the inlet mean velocity, r_o the jet radius and θ the shear layer momentum thickness.

The Reynolds number was set to $Re_D = U_j D/\nu = 6.5 \times 10^4$ and the Mach number to $M = U_j/c_o = 0.90$, where $D = 2r_o$ is the jet diameter, ν the kinematic viscosity and c_o the ambient sound speed. The choise of this Mach number may be justified by the considerable amount of numerical and experimental studies at similar flow conditions. The Reynolds number adopted ($Re_D = 6.5 \times 10^4$) is an intermediate value between jets obtained by DNS ($Re_D < 10^3$) and experimentally ($Re_D > 10^5$). The inlet shear-layer momentum thickness was set to $\theta = 0.05r_o$, which authorizes turbulence development between the nozzle exit and the end of potential core. The mesh was discretized in Cartesian coordinates with $255^3 \approx 16.6$ millions points. The physical domain extends in the streamwise direction from the jet exit until to $60r_o$ and from $-20r_o$ to $20r_o$ in the cross-stream directions. A buffer zone of aerodynamic dissipation/acoustic absorption, with additional grid stretching, was applied just downstream of the physical domain until to $74r_o$, to damp large scale structures of turbulence before they interact with the outflow boundary and minimize spurious wave reflections at the outflow boundary.

3.1 Boundary conditions and buffer zone treatments

In this work, boundaries conditions and *buffer* zone treatments especially adapted for aeroacoustic computations were prescribed by a conceptual model based on the characteristic analysis (Thompson, K. W., 1990) and a non-conservative characteristic-based formulation (Sesterhenn, J., 2001) of compressible Navier-Stokes equations

$$\frac{\partial p}{\partial t} = -\frac{\rho c}{2}((X^+ - X^-) + (Y^+ + Y^-) + (Z^+ - Z^-)) + \frac{p}{C_v}\left(\frac{\partial s}{\partial t} + X^s + Y^s + Z^s\right) \tag{16}$$

$$\frac{\partial u}{\partial t} = -\left(\frac{1}{2}(X^+ - X^-) + Y^u + Z^u\right) + \frac{1}{\rho}\frac{\partial \tau_{1j}}{\partial x_j} \tag{17}$$

$$\frac{\partial v}{\partial t} = -\left(\frac{1}{2}(Y^+ - Y^-) + X^v + Z^v\right) + \frac{1}{\rho}\frac{\partial \tau_{2j}}{\partial x_j} \tag{18}$$

$$\frac{\partial w}{\partial t} = -\left(\frac{1}{2}(Z^+ - Z^-) + X^w + Y^w\right) + \frac{1}{\rho}\frac{\partial \tau_{3j}}{\partial x_j} \tag{19}$$

$$\frac{\partial s}{\partial t} = -(X^s + Y^s + Z^s) + \frac{R}{p}\left(-\frac{\partial q_i}{\partial x_i} + \Phi\right) \tag{20}$$

The wave modal structure of this formulation decomposes small-scale fluctuations of wavy nature into three wave modes of propagation:

- Acoustic waves:

$$X^\pm = (u + c)\left(\frac{1}{\rho c}\frac{\partial p}{\partial x} \pm \frac{\partial u}{\partial x}\right), \quad Y^\pm = (v + c)\left(\frac{1}{\rho c}\frac{\partial p}{\partial y} \pm \frac{\partial v}{\partial y}\right) \quad \text{e} \quad Z^\pm = (w + c)\left(\frac{1}{\rho c}\frac{\partial p}{\partial z} \pm \frac{\partial w}{\partial z}\right) \tag{21}$$

- Entropy waves:

$$X^s = u\frac{\partial s}{\partial x}, \quad Y^s = v\frac{\partial s}{\partial y} \quad \text{e} \quad Z^s = w\frac{\partial s}{\partial z} \tag{22}$$

- Vorticity waves:

$$X^v = u\frac{\partial v}{\partial x}, \quad Y^u = v\frac{\partial u}{\partial y}, \quad \text{e} \quad Z^u = w\frac{\partial u}{\partial z} \tag{23}$$

Boundary conditions. The conceptual model based on the characteristic analysis (Thompson, K. W., 1990) gives the essence of this wave modal approach for prescribing boundary conditions. By the conceptual model, outgoing waves are completely determined by the flow governing equations, with data contained within and at the boundaries of domain, while the behaviour of incoming waves is specified by boundary conditions. As the physical domain must be large enough to allow wave propagation in regions of far-field where the deviations of reference flow are of order of acoustic fluctuations, non-reflecting boundary conditions may be prescribed by simply setting to zero incoming acoustic waves at lateral and outflow boundaries. At the inflow boundary were considered constant entropy, total energy and cross-stream velocities. However, instead of imposing conditions to these quantities, characteristic-based boundary conditions were specified by forcing their time derivatives to zero: (i) $\partial s/\partial t = 0$, (ii) $\partial H/\partial t = 0$, (iii) $\partial v/\partial t = 0$ and (iv) $\partial w/\partial t = 0$.

The entropy equation (20) together with condition (i) allows to solve for the unknown inlet entropy wave

$$X^s = \frac{R}{p}\left(-\frac{\partial q_i}{\partial x_i} + \Phi\right) - Y^s - Z^s \tag{24}$$

The application of condition (ii) in the definition of enthalpy: $H = E + pV$, results

$$\frac{\partial H}{\partial t} = T\frac{\partial s}{\partial t} + \frac{1}{\rho}\frac{\partial p}{\partial t} + u\frac{\partial u}{\partial t} = 0 \tag{25}$$

where E, p and V are the energy, pressure and volume of the system, respectively. The use of condition (i) in Eq. (25) gives the following expression

$$\frac{\partial p}{\partial t} + \rho u\frac{\partial u}{\partial t} = 0 \tag{26}$$

The substitution in Eq. (26) of the momentum and pressure transport equations (Eqs. (16) and (17)) gives the unknown inlet incoming acoustic wave

$$X^+ = \frac{2u}{u + c}\left(\frac{1}{2}X^- - Y^u + \frac{1}{\rho}\left(\frac{\partial \tau_{xx}}{\partial x} + \frac{\partial \tau_{xy}}{\partial y}\right) - \frac{c}{2u}(X^- + Y^+ + Y^-) + \frac{p}{\rho u C_v} + (X^s + Y^s)\right) \tag{27}$$

Finally, the application of conditions (iii) and (iv), respectively, in the momentum transport equations (18) and (19) gives the unknown inlet vorticity wave

$$X^v = -\frac{1}{2}\left(Y^+ - Y^+ + Z^+ - Z^-\right) + \frac{1}{\rho}\left(\frac{\partial \tau_{2j}}{\partial x_j} + \frac{\partial \tau_{3j}}{\partial x_j}\right) \tag{28}$$

Buffer zone treatments. A *buffer* zone of aerodynamic dissipation and acoustic absorption was constructed just downstream of the physical domain. To help on the artificial dissipation process, the grid was gradually stretched in the *buffer* zone. Similarly to Colonius, T. and Lele, S. K. and Moin P. (1993), large-scale vortical and entropic structures of the flow were dissipated inside the *buffer* zone before they interact with the outflow boundary by adding artificial damping terms to the flow governing equations:

$$\left.\frac{\partial \mathbf{Q}}{\partial t}\right|_{dp} = \frac{\partial \mathbf{Q}}{\partial t} - \sigma_{dp}\mathbf{Q}' \tag{29}$$

where $\mathbf{Q}$ is the solution vector $[u,p]$ and $\frac{\partial \mathbf{Q}}{\partial t}$ time derivatives computed by Eqs. (16) and (17). σ_{dp} is an damping function defined as

$$\sigma_{dp}(r) = \frac{1}{4}\left(1 + \tanh\left(a_o \frac{r - 2r_o}{2\theta}\right)\right) \tag{30}$$

with $r^2 = x^2 + y^2$ and $a_o = 0.575$. The disturbance $\mathbf{Q}'$ in Eqs. (29) is computed at each time step as follows

$$\mathbf{Q}'_{(t)} = \mathbf{Q}_{(t)} - \left(\alpha\bar{\mathbf{Q}}_{(t-1)} + (1-\alpha)\mathbf{Q}_{(t)}\right) \tag{31}$$

where $\bar{\mathbf{Q}}_{(t-1)}$ is a mean flow solution computed in the previous time step and $\alpha = 0.90$.

Additionally, an efficient acoustic absorbing condition (Moser, C. A. S. and Lamballais, E. and Gervais, Y., 2006) was gradually applied inside the *buffer* zone to minimize high-frequency spurious wave reflections at the outflow boundary, by adding artificial absorbing terms to the flow governing equations

$$\left.\frac{\partial \mathbf{Q}}{\partial t}\right|_{ab} = \sigma_{ab}\left.\frac{\partial \mathbf{Q}}{\partial t}\right|_{X^-=0} + (1-\sigma_{ab})\frac{\partial \mathbf{Q}}{\partial t} \tag{32}$$

where $\mathbf{Q}$ is the solution vector $[u,p]$ and $\frac{\partial \mathbf{Q}}{\partial t}$ time derivatives computed by Eqs. (16) and (17). σ_{ab} is an absorbing function defined as

$$\sigma_{ab} = \frac{r}{2}(1 + \tanh(\alpha(x - x_o))), \tag{33}$$

with $r = 1$, $\alpha = 0.05$, $x_o = 0.90L_x$ and $\{0 \le \sigma_{ab}(x) \le 1\}$ for $\{x_{ab} \le x \le L_x\}$, where L_x is the length of the computational domain. As at the beginning of the *buffer* zone, $x = x_{ab}$ and $\sigma_{ab} = 0$, Eq. (32) reduces to

$$\left.\frac{\partial \mathbf{Q}}{\partial t}\right|_{ab} = \frac{\partial \mathbf{Q}}{\partial t} \tag{34}$$

Whereas, at the end of *buffer* zone, $x = L_x$ and $\sigma_{ab} = 1$. Thus, at the outflow boundary Eq. (32) is given by

$$\left.\frac{\partial \mathbf{Q}}{\partial t}\right|_{ab} = \sigma_{ab}\left.\frac{\partial \mathbf{Q}}{\partial t}\right|_{X^-=0} \tag{35}$$

Reflections of spurious waves at the inlet were minimized by the application of an acoustic absorbing *buffer* zone (Moser, C. A. S. and Lamballais, E. and Gervais, Y., 2006) in the shear-layer region near the inflow boundary.

4. NUMERICAL RESULTS

Mean flow dynamic characteristics of a Mach 0.9 unforced jet at Reynolds number 65,000 were investigated by an implicit LES method for a considerably large extent of the computational domain. Similarly to forced jets (Moser, C. A. S. and Medeiros, M. A. F., 2012), the mean streamwise velocity profiles U/U_j shown in Fig.3(a) exhibit the well-known top-hat shape inside the potential core region, at the streamwise locations $x/r_o = 5$ and 10. Whereas in the turbulence mixing region, for $x/r_o \ge 15$, the profiles were strongly reduced in magnitude and gradually enlarged in the cross-stream direction. The profiles of the normalized mean velocity U/U_c represented in Fig.3(b) as a function of the axial distance scaled by the jet-half width ($x/r_{1/2}$) exhibit very good self-similarity, since they almost perfectly collapse onto each other. The small unmatched differences between the profiles were due to the mean flow statistics that were not yet fully converged, requiring longer time of simulation.
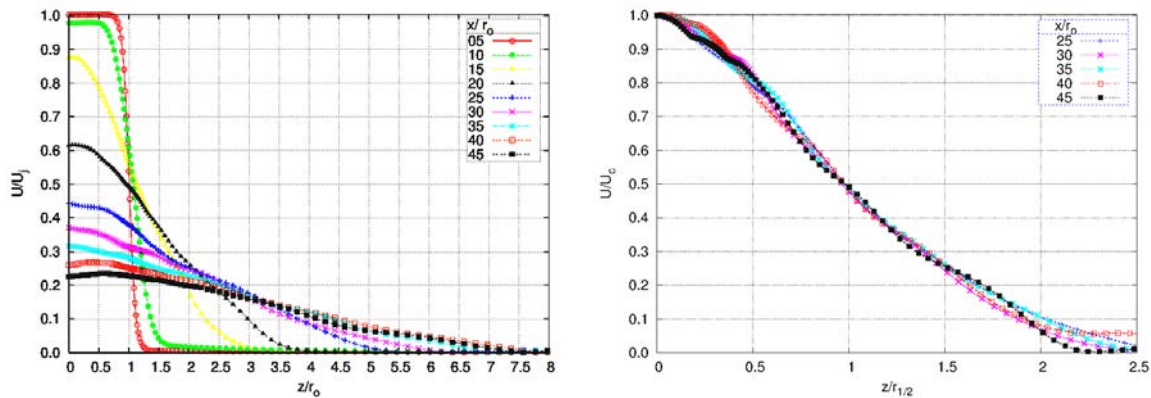
Figure 3. Cross-stream profiles of mean streamwise velocity U taken at different streamwise locations x/r_o and for different normalizations: (a) U/U_j scaled by the normalized distance z/r_o and (b) U/U_c scaled by the normalized distance $z/r_{1/2}$, where $r_{1/2}$ is the jet-half width.

The spatial evolution of the jet width and lateral spreading, depicted in Fig. 4 by instantaneous isocontours of the mean streamwise velocity U/U_c, allows to distinguished three regions: the low-speed (blue), the medium-speed (red) and the high-speed (yellow). In the high-speed turbulence mixing region, the jet width was significantly reduced by strong interactions of large-scale vortical structures across the jet column (Samimy, M. and Kim, J. -H. and Kastner, J. and Adamovich, I. and Utkin, Y., 2007). In addition, the vortex-vortex interaction across the jet column seems to be the major factor related to the mean centreline velocity decay near the end of potential core and the linear increase of jet width in the medium-speed region. The entrainment of ambient fluid into the jet flow and the ejection of jet fluid into the ambient induces the significant increase of lateral spreading in the low-speed region.
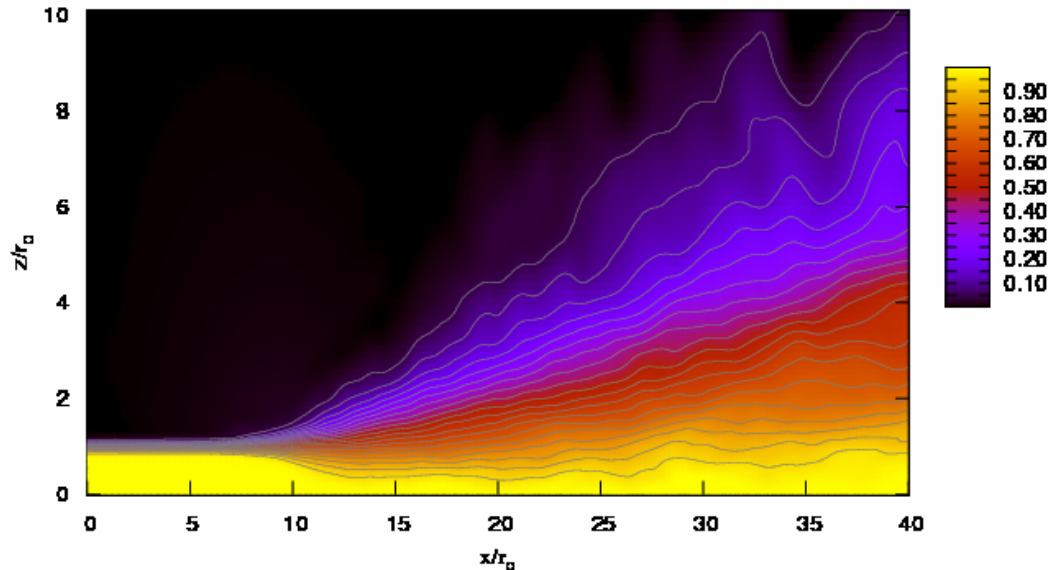

Figure 4. **Evolution of jet growth width and spreading depicted by isocontours of normalized mean streamwise velocity U/U_c. Three regions may be clearly distinguished downstream the end of potential core. In blue the low-speed region** ($0.05 \leq U/U_c < 0.40$**), in red the medium-speed region** ($0.40 \leq U/U_c \leq 0.90$**) and in yellow the high-speed region** ($0.90 < U/U_c \leq 1.00$**). Cross-stream x-z plane at $y = 0$.**

The aerodynamic field of the subsonic unforced jet depicted in Fig.5(a) may be characterized by an orderly quasi-periodic development of Kelvin-Helmholtz instabilities. The large-scale instabilities saturate and collapse into small-scale vortices in the turbulence mixing region, just downstream of potential core. The examination of the acoustic field represented in Fig.5(b) shows that the low velocity fluctuation levels observed close to the jet inlet seem to be unable to start-up the self-sustained shear-layer instabilities or induce significant spurious wave reflections at the inlet. By the analysis of both aerodynamic and acoustic fields it is also possible to verify that the dominant noise source radiates from the shear layer region localized near the end of potential core. As already observed by several studies of forced jets, in the unforced jet the noise radiates to the acoustic field at small angles relative to the jet axis and is highly directive.
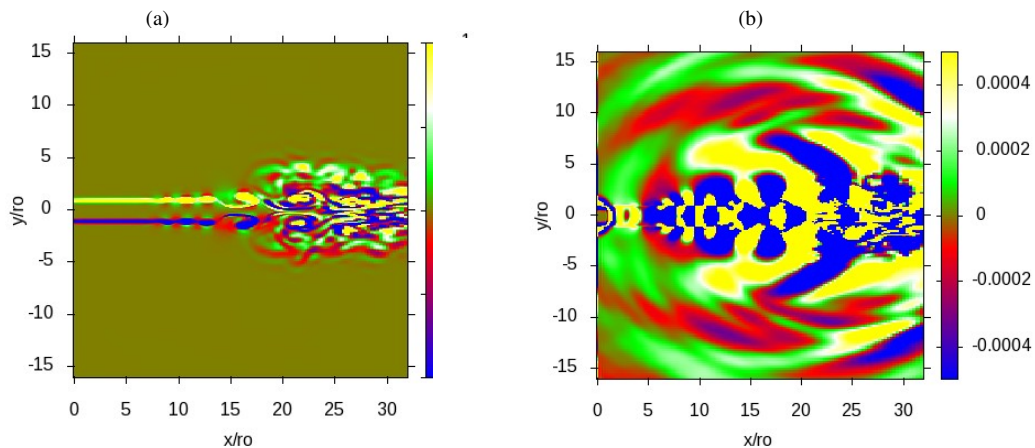
C. Moser, M. Medeiros
Analysis of Jet Shear Layer Self-Sustained Instability Effects

Figure 5. **Snapshots of the aerodynamic (a) and acoustic (b) fields represented, respectively, by the vorticity and divergence. Physical domain includes the *buffer* zone of acoustic absorption, near the jet inlet.**

Streamwise velocity fluctuations u' were evaluated in Fig.6 at five instants of time and at different positions. The snapshot of Fig.6 (left) shows that close to the jet exit the velocity fluctuation is very low, $u'(x/r_o \approx 1) \approx O(10^{-5})$, and increases exponentially in the downstream direction until to attain values of order $O(10^{-3})$ for $x/r_o \approx 4$. As shows Fig.6 (right), u' continuous to increase exponentially along the potential core until to attain values of order $O(10^{-1})$, with saturation of shear-layer instabilities at the end of potential core ($x/r_o \approx 12$). However, even that close to the jet inlet the values of velocity fluctuations are significantly smaller than the values at the end of potential core, i. e. $u'(x/r_o \approx 1) \approx 10^{-5} << u'(x/r_o \approx 12) \approx 10^{-1}$, one may yet expect some small-scale *feedback* effects, which could be originated by flow-acoustics interactions with the inflow boundary conditions and/or with the near-inlet acoustic absorbing *buffer* zone.
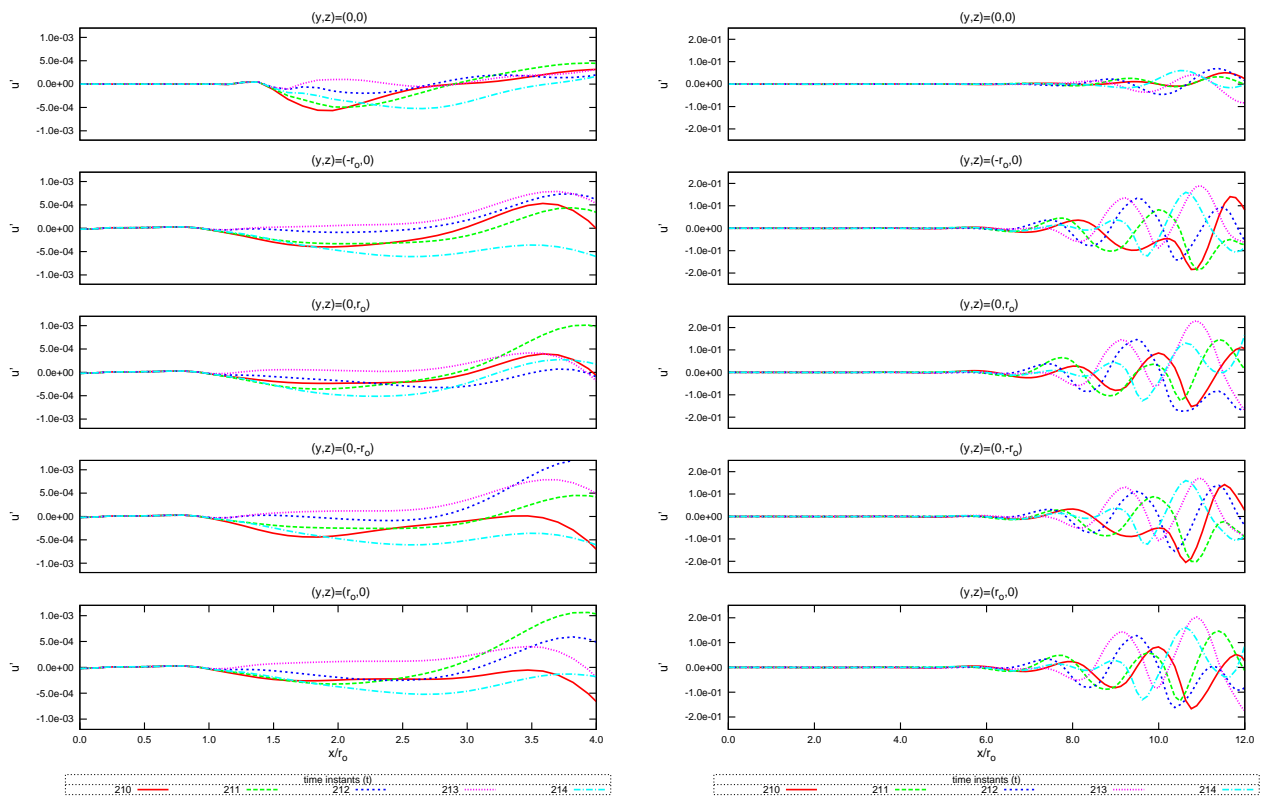

Figure 6. **Snapshots of velocity fluctuations u' taken at five instants of time t at jet axis $(x/r_o, 0, 0)$ and shear-layer: $(x/r_o, -1, 0)$, $(x/r_o, 0, 1)$, $(x/r_o, 0, -1)$ and $u'(x/r_o, 1, 0)$. Detail of the region close to the jet inlet for $(0 \leq x/r_o \leq 4)$ (left) and the potential core region for $(0 \leq x/r_o \leq 12)$ (right), where r_o is the jet radius.**

In figure 7 is represented the time evolution of velocity fluctuations u' spatially averaged with four measurements taken from the jet shear-layer at the streamwise locations $x/r_o = \{3, 6, \ldots, 27, 30\}$. Close to the jet inlet (for $x/r_o = 3$) the velocity fluctuations presents a random-fashion pattern similar to the one observed in the fully developed turbulence mixing region (for $(x/r_o \geq 24)$, which contrasts with the orderly quasi-periodic pattern developed in the jet potential core (for $12 \leq x/r_o \leq 18$) suggesting the existence of a self-sustained *feedback* mechanism induced by close interactions of vortices formed in the jet shear layer. This mechanism seems to be independent of inflow boundary conditions and the near-inlet *buffer* zone.
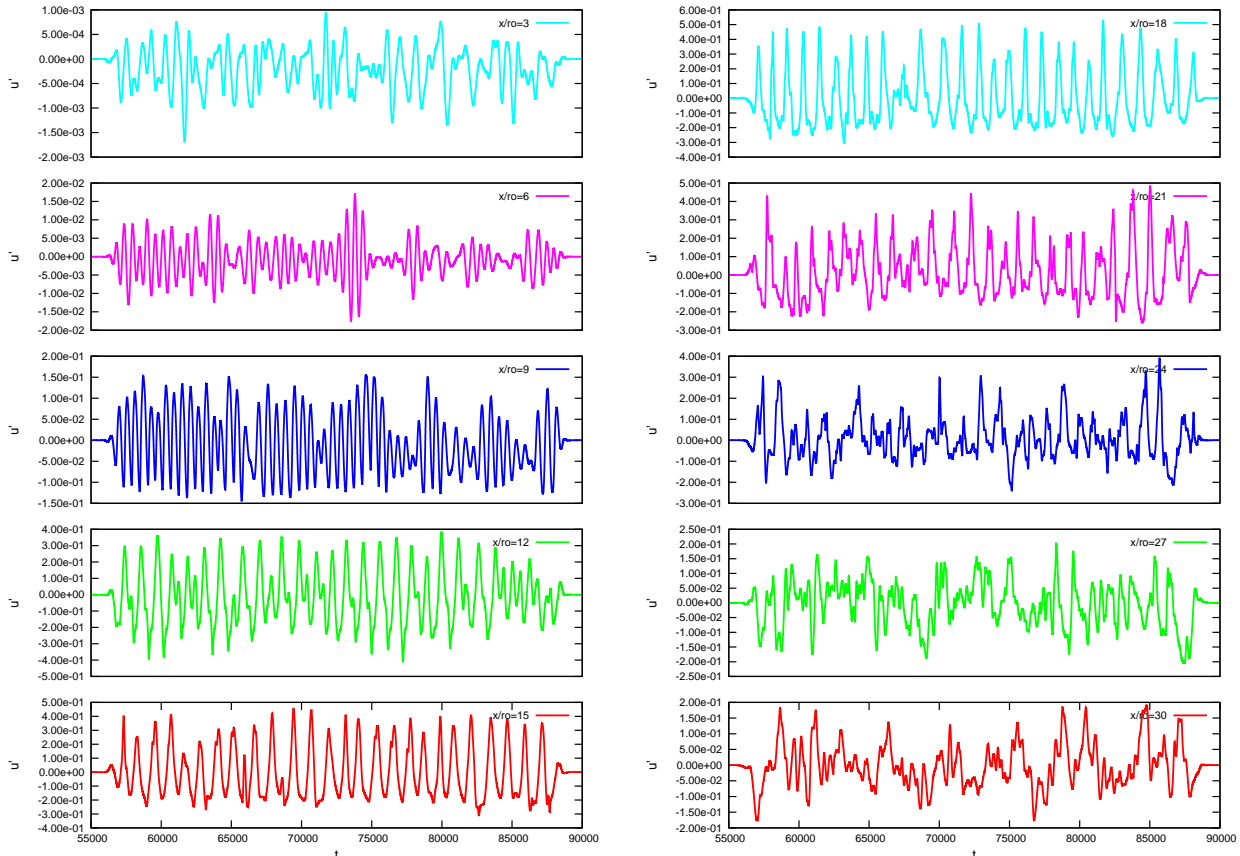

Figure 7. **Time evolution of velocity fluctuations u' spatially averaged with measurements taken from the jet shear-layer:** $(y/r_o, z/r_o) = (-1, 0), (0, 1), (0, -1), (1, 0)$ **at different streamwise locations.**

5. CONCLUSIONS

The influence of self-sustained instabilities on the aerodynamic noise radiated by a subsonic unforced isothermal jet was investigated by an implicit large-eddy simulation method. The low disturbance level of flow velocity fluctuations detected close to the jet inlet seems to be unable to start-up the development of self-sustained shear-layer instabilities or induce significant spurious wave reflections at the inlet. Distinct patterns of velocity fluctuations were observed in the jet shear layer. Close to the jet inlet was detected a random-fashion pattern similar to the one observed in the turbulence mixing region, which contrasts with the orderly quasi-periodic pattern observed in the potential core. This suggests the existence of a self-sustained *feedback* mechanism induced by close interactions of vortices formed in the jet shear layer. Local instability properties, such as turbulence intensities and natural frequency of instability waves, will be evaluated by comparing the ongoing work with numerical and experimental results obtained from the literature at similar flow conditions.

6. ACKNOWLEDGEMENTS

7. REFERENCES

Bodony, D. J. and Lele, S. K., 2002. "Large eddy simulation of turbulent jets and progress towards a subgrid scale noise model". *Proceedings of International Workshop on LES for Acoustics, DGLR, Gottingen, Germany.*

Bogey, C. and Bailly, C., 2005a. "Effects of inflow conditions and forcing on subsonic jet flows and noise". *AIAA J.*

Colonius, T. and Lele, S. K. and Moin P., 1993. "Boundary condition for direct computation of aerodynamic sound generation". *AIAA journal*, Vol. 31, No. 9, pp. 1574–1582.

Gaitonde, D. V. and Visbal, M. R., 1998. "High-order schemes for Navier-Stokes equations Algorithm and implementation into FDL3DI". *Technical Report AFRLVA-WP-TR-1998-3060, Air Force Research Laboratory, Wright-Patterson, AFB.*

Gaitonde, D. V. and Visbal, M. R., 1999. "Further development of a Navier-Stokes solution procedure based on higher-order formulas". *AIAA Paper No. 99-0557.*

Galdi, G. P., 2000. In *Lectures in Mathematical Fluid Dynamics*. Birkhäuser-Verlag, Basel, Switzerland.

Germano, M. and Piomelli, U. and Moin, P., 1991. "A dynamic subgrid-scale eddy viscosity model". *Phys. Fluids A*, Vol. 3, pp. 1760–1765.

Lele, S. K., 1992. "Compact finite difference schemes with spectral like resolution". *J. Comput. Phys.*, Vol. 103, pp. 16–42.

Leonard, A., 1974. "Energy cascade in large eddy simulations of turbulent fluid flows". *Adv. Geophys*, Vol. 18A, pp. 237–248.

Moser, C. A. S. and Lamballais, E. and Gervais, Y., 2006. "Direct computation of the sound generated by isothermal and non-isothermal mixing layers". *The 12th AIAA/CEAS Aeroacoustic conference, AIAA Paper 2006-2447.*

Moser, C. A. S. and Medeiros, M. A. F., 2012. "Non-conservative implicit large-eddy simulation method for predicting the noise radiated by subsonic jets". *The 18th AIAA/CEAS Aeroacoustics Conference, Colorado Springs, Colorado, USA.*

Sagaut, P., 2001. "Large eddy simulation for incompressible flows". *Springer Verlag.*

Samimy, M. and Kim, J. -H. and Kastner, J. and Adamovich, I. and Utkin, Y., 2007. "Active control of high-speed and high-Reynolds-number jets using plasma actuators". *J. Fluid Mech.*, Vol. 578, pp. 305–330.

Sesterhenn, J., 2001. "A characteristic-type formulation of the Navier-Stokes equations for high order upwind schemes". *Comput. Fluids*, Vol. 30, pp. 37–67.

Stolz, S. and Adams, N. A., 1999. "An approximate deconvolution procedure for large eddy simulation". *Phys. Fluids A*, Vol. 11, pp. 1699–1701.

Thompson, K. W., 1990. "Time-dependent boundary conditions for hyperbolic systems, II." *J. Comput. Phys.*, Vol. 89, pp. 439–461.

8. RESPONSIBILITY NOTICE

The authors are the only responsible for the printed material included in this paper.